
An Elastic Shape Variational Autoencoder for Skeleton Pose Trajectories

Arafat Rahman^{1*}, Shashwat Kumar^{2*}, Laura E. Barnes¹, Anuj Srivastava³

¹Systems and Information Engineering, University of Virginia, Charlottesville, VA, USA

²Biomedical Engineering, Johns Hopkins University, Baltimore, MD, USA

³Dept. of Applied Mathematics and Statistics, Johns Hopkins University, Baltimore, MD, USA

{jgh6ds, lb3dp}@virginia.edu
skuma118@jh.edu, anuj.srivastava@jhu.edu

Abstract

Deep generative models provide flexible frameworks for modeling complex, structured data such as images, videos, 3D objects, and texts. However, when applied to sequences of human skeletons, standard variational autoencoders (VAEs) often allocate substantial capacity to nuisance factors—such as camera orientation, subject scale, viewpoint, and execution speed—rather than the intrinsic geometry of shapes and their motion. We propose the Elastic Shape - Variational Autoencoder (ES-VAE), a geometry-aware generative model for skeletal trajectories that leverages the transported square-root velocity field (TSRVF) representation on Kendall’s shape manifold. This representation inherently removes rigid translations, rotations, and global scaling of shapes, and temporal rate variability of sequences, isolating the underlying shape dynamics. The ES-VAE encoder maps skeletal sequences to a low-dimensional latent space incorporating the Riemannian logarithm map, while the decoder reconstructs sequences using the corresponding exponential map. We demonstrate the effectiveness of ES-VAE on two datasets. First, we analyze skeletal gait cycles to predict clinical mobility scores and classify subjects into healthy and post-stroke groups. Second, we evaluate action recognition on the NTU RGB+D dataset. Across both settings, ES-VAE consistently outperforms standard VAEs and a range of sequence modeling baselines, including temporal convolutional networks, transformers, and graph convolutional networks. More broadly, ES-VAE provides a principled framework for learning generative models of longitudinal data on pose shape manifolds, offering improved latent representation and downstream performance compared to existing deep learning approaches.

1 Introduction

Skeleton trajectories have become ubiquitous in activity recognition [Sun et al., 2022], gait recognition [Fan et al., 2024], automatic motion assessment [Hakim and Shimshoni, 2019], and disease severity prediction [Adeli et al., 2024]. Despite the advances in data collection, extracting meaningful features from such high-dimensional data is far from straightforward.

One approach to learn interpretable representations from high dimensional data is to use variational autoencoders (VAE) [Kingma and Welling, 2013]. These have proven to be useful in applications ranging from computer vision [Harvey et al., 2022] to computational biology [Lopez et al., 2018]. Applied to pose data, though, a standard VAE devotes a large part of its capacity to irrelevant dimensions, *e.g.*, camera orientation, sensor distance, body size and rate at which the activity is

*Equal contribution.

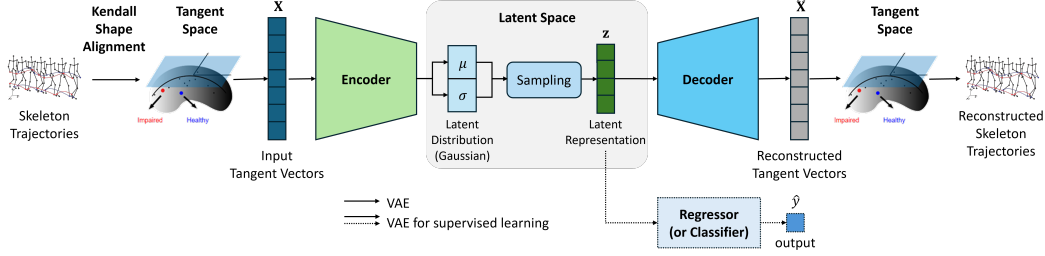


Figure 1: Overview of the Elastic Shape VAE architecture. Raw skeleton trajectories are embedded in Kendall shape space by removing translation, scale, and rotation. Temporal alignment via the transported SRVF removes rate variability. The Riemannian VAE encoder maps tangent vectors to a low-dimensional latent code z , and the decoder maps z back through the tangent space and onto the shape manifold via the exponential map.

performed. These nuisance variables are unavoidable in naturalistic gait or activity recording setups where participants walk or perform activity at their own pace and starting position [Van Crieking et al., 2023]. However, they play no role in deriving inferences about activity classification or labeling. In fact, it is common in traditional shape analysis [Dryden and Mardia, 2016] to remove certain nuisance transformations before applying statistical analyses. The question is how to perform this removal while involving powerful ML and AI techniques that are often geared towards Euclidean variables.

In order to develop an AI-based technique for analyzing shape sequences, while focusing directly on shapes and shape dynamics, we represent skeleton trajectories as stochastic processes in *Kendall shape space* [Kendall et al., 1999]. The representation automatically quotients out translations, rotations, and scaling of individual shapes. We pair this with the *transported square-root velocity field* (TSRVF) framework [Ben Amor et al., 2016] on shape manifold to remove the temporal rate variability (activity speed) of sequences. The resulting model, *Elastic Shape VAE* (ES-VAE), is invariant to these confounders by design while focusing on shape dynamics in form of meaningful latent representations. Figure 1 shows the overview of the full architecture.

1.1 Contributions

1. We introduce Elastic Shape VAE, a Riemannian VAE that full embeds skeleton trajectories – represented by transported SRVFs on Kendall shape space – into low-dimensional latent space. This representation results in complete invariance to shape translations, rotations, scaling, and speed profiles of activities.
2. Using the unit sphere \mathbb{S}^2 as an example, we show that Elastic Shape VAE approximates non-geodesic, one-dimensional submanifolds better than such popular ideas Euclidean PCA, Euclidean VAE, and tangent-space PCA. This demonstrates that modeling directly on the manifold preserves nonlinear geometric structure that is lost under Euclidean approximations.
3. On a clinical dataset of 155 participants (111 healthy, 44 stroke), we demonstrate that the learned latent dimensions: (1) map to interpretable gait features (stride length, limb stiffness, arm variability), (2) correlate highly with clinical scores, and (3) outperform other classical and deep learning approaches for predicting stroke severity.
4. On a representative subset of activity recognition dataset, the learned latent dimensions similarly outperformed other classical and deep learning approaches in classifying different activities.

The remainder of this paper is organized as follows. Section 2 reviews related work. Section 3 presents the mathematical framework. Section 4 describes the experimental setup. Section 5 presents the results. Section 6 discusses the findings and limitations, and Section 7 concludes.

2 Related Literature

Riemannian and Geometric Deep Learning: Deep generative models have been pushed beyond Euclidean space in several ways. Miolane and Holmes [2020] introduced the Riemannian VAE, where the decoder maps latent codes through the tangent space at a base point and then onto the manifold via the exponential map. The network therefore only has to learn the residual, not the full manifold geometry. Chadebec and Allasonnière [2022] used inverse posterior covariances to define a Riemannian metric in the VAE latent space and then used geometry-aware sampling to improve generation compared to standard Gaussian sampling. On the shape-modeling side, Bône et al. [2019] built diffeomorphic autoencoders for neuroimaging atlas construction. Dummer et al. [2024, 2023] developed Riemannian diffeomorphic autoencoders with implicit neural representations. Gatti et al. [2025] benchmarked neural shape models on 3D femur data, where hybrid explicit-implicit models beat classical statistical shape models. Fu et al. [2025] combined Riemannian VAEs with geodesic-aware Transformers for EEG decoding. All of these operate on general manifolds. We instead work on *Kendall shape space*, which is purpose-built for skeleton data: translation, rotation, and scale invariance come from the geometric construction itself, so there is no need for data augmentation or learned invariances. Vadgama et al. [2022] used a Kendall pre-shape latent representation, learning landmark-like codes from images using VAE. In contrast, our inputs are skeletons, whose joints are already landmarks, so we model them directly in Kendall shape space.

Shape Analysis of Skeletal Data: Several works have been done on the shape analysis of skeleton trajectories. Ben Amor et al. [2016] used the transported SRVF framework on Kendall shape space for rate-invariant action recognition. Hosni et al. [2018] extended the idea to 3D gait recognition with functional PCA on Kendall shape space. Friji et al. [2021] paired Kendall shape representations with a CNN-LSTM classifier for skeleton action recognition and added a differentiable transformation layer to handle both rigid and non-rigid normalizations. These are all discriminative approaches (classification). We instead integrate shape-space invariances into a VAE, yielding an interpretable latent embedding of skeleton shape trajectories that suppresses nuisance variation. While there have been several papers on AI-based encoding of *static* shapes, this is the first effort to encode full shape trajectories in a manner that is invariant to all spatio-temporal nuisance variables. Additional related works are given in Appendix Section A.

3 Methodology

In this section, we utilize the geometry of Kendall’s shape representation and develop low-dimensional VAE-based representations of human skeleton and their evolutions.

3.1 Kendall Shape Representations

Each human skeleton is made of k landmarks in \mathbb{R}^m where $m = 3$ is the ambient dimension. We represent a skeleton in a matrix form $X \in \mathbb{R}^{k \times m}$. The inner product between any two configurations $X_1, X_2 \in \mathbb{R}^{k \times m}$ is $\langle X_1, X_2 \rangle = \text{tr}(X_1^\top X_2)$. Following Kendall et al. [1999], we define the *shape* of a skeleton as the geometric information that remains after removing position, orientation, and size. The full process is described below.

Removing translation: To remove translation, we simply center each configuration by subtracting the column means, yielding the centered configuration space:

$$V_m^k = \left\{ X \in \mathbb{R}^{k \times m} : \sum_{i=1}^k X_{i,:} = \mathbf{0} \right\}. \quad (1)$$

Removing scale. We normalize each centered configuration to unit Frobenius norm, yielding the *preshape space*: $S_m^k = \{X \in V_m^k : \|X\|_F = 1\}$. The unit-norm constraint endows the preshape space with a spherical geometry. We impose the standard Euclidean metric as a Riemannian metric on S_m^k which leads to the geodesic distance $d_S(X_1, X_2) = \cos^{-1}(\langle X_1, X_2 \rangle)$.

Removing rotation. Even after removing position and scale, orientation remains as a nuisance variable. The special orthogonal group $\text{SO}(m) = \{R \in \mathbb{R}^{m \times m} : R^\top R = I, \det(R) = 1\}$ acts on preshape space by right multiplication: $X \mapsto XR$. This action preserves the preshape metric, since for tangent vectors $u, v \in T_X S_m^k$: $\langle uR, vR \rangle = \text{tr}(R^\top u^\top vR) = \text{tr}(u^\top v) = \langle u, v \rangle$.

We define an equivalence relation: $X_1 \sim X_2$ if and only if $X_2 = X_1 R$ for some $R \in \text{SO}(m)$. *Kendall shape space* is the quotient: $\Sigma_m^k = S_m^k / \text{SO}(m) = \{[X] | X \in S_m^k\}$, where an equivalence class is defined as $[X] = \{XO : O \in \text{SO}(m)\}$.

Away from singularities, the quotient map $\pi : S_m^k \rightarrow \Sigma_m^k$, given by $\pi(X) = [X]$, is a Riemannian submersion and induces a metric on Σ_m^k from S_m^k . The geodesic distance between two shapes $[X_1], [X_2] \in \Sigma_m^k$ is:

$$d_{\Sigma_m^k}([X_1], [X_2]) = \inf_{R \in \text{SO}(m)} d_S(X_1, X_2 R), \quad (2)$$

where d_S is as defined earlier. The optimal rotation R^* is found via Orthogonal Procrustes Analysis (OPA).

Exponential and logarithmic maps. Given a base point $\nu \in S_m^k$ and a tangent vector $w \in T_\nu S_m^k$, the exponential map on the preshape sphere is:

$$\text{Exp}_\nu(w) = \cos(\|w\|_F) \nu + \sin(\|w\|_F) \frac{w}{\|w\|_F}. \quad (3)$$

The logarithmic map, which maps a point $X \in S_m^k$ to a tangent vector at ν , is given by:

$$\text{Log}_\nu(X) = \frac{\theta}{\sin \theta} (X - \cos(\theta) \nu), \text{ where } \theta = \cos^{-1}(\langle \nu, X \rangle). \quad (4)$$

3.2 Transported SRVF and Temporal Alignment

A skeleton trajectory is a curve $\beta : [0, 1] \rightarrow \Sigma_m^k$ parameterized by time. The set of all such smooth trajectories is given by \mathcal{M} . For any point $\mu \in \mathcal{M}$, the tangent space $T_\mu \mathcal{M} = \prod_t T_{\mu(t)} \Sigma_m^k$. The log and exponential maps for full trajectories are defined using their analogs at each time t . That is: $\text{Log}_\mu(\beta_n) = \{\text{Log}_{\mu(t)}(\beta_n(t)) : t \in [0, 1]\}$ and $\text{Exp}_\mu(v) = \{\text{Exp}_{\mu(t)}(v(t)) : t \in [0, 1]\}$.

Different participants may walk at different speeds, introducing rate variability. We handle this using the *transported square-root velocity function* (TSRVF) [Ben Amor et al., 2016].

For a trajectory $\beta \in \mathcal{M}$, we compute the covariant derivative $\dot{\beta}(t)$ via: $\dot{\beta}(t) \approx \frac{\text{Log}_{\beta(t)}(\beta(t+\Delta t))}{\Delta t}$, and parallel transport the resulting tangent vectors to a common reference point $c \in \Sigma_m^k$. As common reference point we used Fréchet mean. The TSRVF $q : [0, 1] \rightarrow T_c \Sigma_m^k$ is then:

$$q(t) = \frac{(\dot{\beta}(t))_{\beta(t) \rightarrow c}}{\sqrt{\|(\dot{\beta}(t))_{\beta(t) \rightarrow c}\|_2}}, \quad (5)$$

where the subscript denotes parallel transport from $\beta(t)$ to c .

Temporal alignment. Let Γ denote the set of orientation-preserving diffeomorphisms of $[0, 1]$ (reparameterizations). For a trajectory β and a $\gamma \in \Gamma$, the composition $\beta \circ \gamma$ denotes the same set of points, but traversed at a rate governed by γ . For any two trajectories β_n and μ , the optimal time warping is:

$$\gamma_n^* = \arg \min_{\gamma \in \Gamma} \int_0^1 \left\| q_\mu(t) - q_{\beta_n}(\gamma(t)) \sqrt{\dot{\gamma}(t)} \right\|_2^2 dt, \quad (6)$$

which is solved via efficient Dynamic Programming Algorithm (DPA) [Bertsekas, 2012]. The aligned trajectory is $\tilde{\beta}_i = \beta_i \circ \gamma_i^*$.

3.3 Mean Trajectory and Registration

Given a collection of skeleton trajectories $\{\beta_n(t)\}_{n=1}^N$ on Kendall shape space, we iteratively compute their Fréchet mean $\mu \in \mathcal{M}$ and simultaneously align and register all trajectories to this mean. This process iterates, alternating between (i) rotationally aligning each shape $\beta_n(t)$, for each n , to the current mean $\mu(t)$ via OPA, (ii) temporally aligning each trajectory β_n to the current mean μ via TSRVF optimization, and (iii) updating the mean, until convergence. While steps (i) and (ii) are discussed earlier, we explain the updating of mean. For each n , we first compute the shooting vectors: $v_n = \text{Log}_\mu(\beta_n)$ and their average $\bar{v} = \frac{1}{N} \sum_{n=1}^N v_n$. We use this mean to update the current mean according to: $\mu \leftarrow \text{Exp}_\mu(\epsilon \bar{v})$, where ϵ is a step size.

The output of this process is the mean trajectory μ and a set of aligned and registered trajectories $\{\tilde{\beta}_n\}$ with corresponding tangent vectors $v_n \in T_\mu \mathcal{M}$ (equivalently, $\{v_n(t) \in T_{\mu(t)} \Sigma_m^k : t \in [0, 1]\}$).

3.4 Riemannian VAE on Shape Space

We use a latent space encoding to impose probability distribution on the trajectory space \mathcal{M} . For a latent space \mathbb{R}^L , let $f_\theta : \mathbb{R}^L \rightarrow T_\mu \mathcal{M}$ denote a neural network mapping from the latent space to the tangent space at μ . Then, each aligned trajectory $\tilde{\beta}_n$ is modeled as a random sample according to:

$$\tilde{\beta}_n \sim \mathcal{N}_{\mathcal{M}}(\text{Exp}_\mu(f_\theta(z_n)), \sigma^2), \quad (7)$$

where $z_n \sim \mathcal{N}(\mathbf{0}, \mathbf{I}_L)$ denote a latent code of dimension L .

Encoder. The encoder takes as input the tangent vector representation $v_n = \text{Log}_\mu(\tilde{\beta}_n)$ and produces the parameters of an approximate posterior:

$$h_\phi(z_n | v_n) = \mathcal{N}(\mu_\phi(v_n), \text{diag}(\sigma_\phi^2(v_n))), \quad (8)$$

where μ_ϕ and σ_ϕ are parameterized by neural networks.

Decoder. The decoder maps the latent code z_n to a tangent vector $f_\theta(z_n) \in T_\mu \mathcal{M}$, which is then projected onto the manifold: $\hat{\beta}_n = \text{Exp}_\mu(f_\theta(z_n))$.

Riemannian Evidence Lower Bound (ELBO). As training objective we used the Riemannian ELBO:

$$\mathcal{L}(\theta, \phi) = \mathbb{E}_{h_\phi(z|v_n)} [\log p_\theta(\tilde{\beta}_n | z)] - \text{KL}(h_\phi(z | v_n) \| p(z)), \quad (9)$$

where the reconstruction term uses the squared geodesic distance on the shape manifold:

$$-\log p_\theta(\tilde{\beta}_n | z) \propto \sum_{t=1}^T d_{\Sigma_m^k}(\tilde{\beta}_n(t), \hat{\beta}_n(t))^2, \quad (10)$$

Here, $\hat{\beta}_n(t)$ is the reconstructed skeleton trajectory and the KL divergence for the diagonal Gaussian encoder against the standard normal prior is:

$$\text{KL}_n = \frac{1}{2} \sum_{j=1}^L (\sigma_j^2(v_n) + \mu_j^2(v_n) - 1 - \log \sigma_j^2(v_n)). \quad (11)$$

The total loss over a mini-batch of N samples is:

$$\mathcal{L} = \frac{1}{N} \sum_{n=1}^N \left(\sum_{t=1}^T d_{\Sigma_m^k}(\tilde{\beta}_n(t), \hat{\beta}_n(t))^2 + \beta_{\text{kl}} \cdot \text{KL}_n \right), \quad (12)$$

where β_{kl} controls the trade-off between reconstruction fidelity and latent regularization. The full derivation is given in Appendix Section B.

4 Experimental Setup

Datasets: We evaluate ES-VAE on two skeleton datasets: a clinical gait stroke dataset for fine-grained continuous prediction and laterality classification, and a curated subset of NTU-60 for action recognition. On the stroke dataset, we predicted Tinetti Performance Oriented Mobility Assessment (POMA) scores and performed three-class classification (left-sided stroke, right-sided stroke, and healthy subject). On NTU-60, we evaluated action recognition on a curated subset of 10 hard-to-classify activities. The full dataset details are given in Appendix Section C.

Implementation Details: The Fréchet mean was computed over 40 iterations with step size $\epsilon = 0.1$ and convergence tolerance 10^{-5} . Rotational alignment was performed via OPA at each iteration, and temporal alignment via dynamic programming on the TSRVF representation. The same alignment pipeline is applied to both datasets; only the input dimensionality and the joint count differ. Details about network architecture, training, inference, and evaluation protocol are provided in Appendix Section D.

Comparison of Different Submanifold Learning Methods

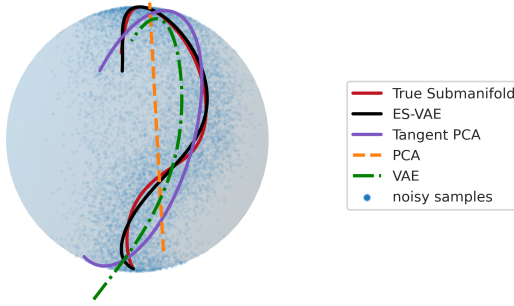


Figure 2: Comparison of submanifold learning methods on synthetic data on \mathbb{S}^2 . Blue points denote noisy samples generated around a true nonlinear submanifold (red) on the sphere. The black curve shows the submanifold learned by ES-VAE. The purple curve shows the Tangent PCA reconstruction projected back onto the sphere. The dashed orange and dash-dotted green curves correspond to standard Euclidean PCA and Euclidean VAE, respectively. ES-VAE most accurately recovers the data’s underlying non-geodesic structure. In contrast, PCA is limited by its linearity, the VAE fails to capture the spherical geometry in the lower region of the sphere, and Tangent PCA is restricted to geodesic trajectories.

Baseline Methods: We compare ES-VAE against a comprehensive set of baselines spanning different categories of input representations:

1. **Raw skeleton methods:** PCA + k -NN, VAE + k -NN, Temporal Convolutional Network (TCN) [Lea et al., 2017], Long Short-Term Memory (LSTM) [Hochreiter and Schmidhuber, 1997], Transformer [Vaswani et al., 2017], and Spatio-Temporal Graph Convolutional Network (ST-GCN) [Yan et al., 2018], Sparse ST-GCN [Xie et al., 2025], and Hyper-Graph Convolutional Network (Hyper-GCN) [Zhou et al., 2025] applied directly to unregistered skeleton sequences.
2. **Joint angle methods:** PCA on gait-normalized joint angles [Cho et al., 2024] + k -NN, and VAE on joint angles + k -NN for stroke dataset as joint angles were available in that dataset only and not in NTU-60 dataset.
3. **Tangent vector methods:** Tangent PCA + k -NN, which applies PCA in the tangent space at the Fréchet mean after Kendall shape alignment (the same alignment used by ES-VAE, but with a linear dimensionality reduction instead of VAE). Additionally we evaluated the six models (TCN, LSTM, Transformer, ST-GCN, Sparse ST-GCN, Hyper-GCN) on tangent-vector inputs.

5 Experimental Results

5.1 Results on Synthetic Data

We first demonstrate the merit of our approach using synthetic data on a unit sphere \mathbb{S}^2 . In this experiment, we generate points along a non-geodesic curve – a one-dimensional submanifold – on \mathbb{S}^2 and used each method to recover that curve (see Figure 2). PCA and classical VAE both work in the ambient Euclidean space. PCA ignores the curvature entirely, while the VAE cannot follow the spherical geometry in the lower portion. Tangent PCA can only follow geodesic paths because it is linear at the base point. ES-VAE better tracks the non-geodesic structure of the data and gives more accurate approximation of the true submanifold.

5.2 Regression Performance on Stroke Dataset

Next, we present results on clinical gait stroke dataset. Table 1 compares performances of all methods on POMA regression. It can be seen that ES-VAE outperforms others with $R^2 = 0.74$, RMSE = 2.82, and Pearson $r = 0.86$ which is clearly better than best raw-skeleton deep learning model (LSTM, $R^2 = 0.64$, RMSE = 3.31), and joint angle PCA ($R^2 = 0.44$). Even relative to Tangent PCA ($R^2 = 0.70$, RMSE = 3.03), the gap shows the value of the nonlinear VAE mapping over a

Table 1: Regression performance for POMA score prediction. Metrics are pooled out-of-fold predictions under subject-wise cross-validation. 95% confidence intervals are obtained via subject-level bootstrap resampling.

Input Representation	Method	RMSE	R^2	Pearson r
Raw Skeleton	TCN	3.82 (3.21–4.30)	0.52 (0.30–0.67)	0.79 (0.73–0.85)
	LSTM	3.31 (2.69–3.79)	0.64 (0.52–0.74)	0.81 (0.74–0.87)
	Transformer	3.93 (3.19–4.50)	0.50 (0.29–0.66)	0.76 (0.69–0.84)
	ST-GCN	3.88 (3.08–4.49)	0.51 (0.34–0.66)	0.72 (0.64–0.82)
	Sparse ST-GCN	3.83 (3.02–4.38)	0.52 (0.37–0.67)	0.74 (0.67–0.83)
	Hyper-GCN	3.57 (2.90–4.07)	0.58 (0.48–0.68)	0.77 (0.71–0.83)
	PCA + k -NN	4.46 (3.91–4.95)	0.35 (0.23–0.44)	0.59 (0.49–0.68)
	VAE + k -NN	4.33 (3.77–4.83)	0.39 (0.26–0.48)	0.62 (0.52–0.71)
Joint Angle	PCA + k -NN	4.13 (3.34–4.72)	0.44 (0.34–0.55)	0.76 (0.67–0.85)
	VAE + k -NN	3.71 (2.87–4.32)	0.55 (0.45–0.67)	0.76 (0.68–0.84)
Tangent Vector	TCN	3.39 (2.79–3.86)	0.62 (0.47–0.75)	0.82 (0.77–0.89)
	LSTM	3.21 (2.58–3.69)	0.66 (0.57–0.75)	0.81 (0.76–0.87)
	Transformer	3.23 (2.52–3.73)	0.66 (0.58–0.75)	0.81 (0.77–0.87)
	ST-GCN	3.51 (2.93–3.99)	0.60 (0.46–0.71)	0.77 (0.69–0.84)
	Sparse ST-GCN	3.36 (2.56–3.88)	0.63 (0.50–0.76)	0.80 (0.72–0.87)
	Hyper-GCN	3.86 (3.09–4.43)	0.51 (0.36–0.65)	0.74 (0.66–0.82)
	Tangent PCA + k -NN	3.03 (2.39–3.48)	0.70 (0.59–0.80)	0.84 (0.78–0.90)
	ES-VAE + k-NN (proposed)	2.82 (2.29–3.21)	0.74 (0.66–0.82)	0.86 (0.82–0.91)

linear projection in the tangent space. Additional results of classification on stroke dataset is given in Appendix Section E.2.

5.3 Classification Performance on NTU-60 Action Recognition Dataset

Table 2 reports ten-class classification on the NTU-60 subset under leave-five-subjects-out (L5SO) cross-validation. With matched architectures and folds, every tangent-vector-input model except Hyper-GCN outperforms its raw-skeleton counterpart, confirming that Kendall shape-space alignment supplies the discriminative signal. ES-VAE + k -NN attains the best macro F1 of 0.56, surpassing other raw-skeleton baselines and the best tangent baseline (Tangent PCA + k -NN at 0.50). This score should not be interpreted as an NTU-60 leaderboard result, since our experiment uses a small, difficult ten-class L5SO subset with only 300 training samples per fold. Instead, the goal is a controlled representation comparison in which the data, folds, model, and k -NN protocol are held fixed. ES-VAE also improves macro F1 by +0.29 over Vanilla VAE (0.56 vs. 0.27) using identical encoder/decoder widths, latent dimension, batch size, and training schedule.

5.4 Modes of Variation of Latent Variables in Stroke Dataset

Figure 3 shows what the first five latent dimensions (z_1 through z_5) actually encode, sorted by decreasing variance. The mean skeleton is drawn in black and the red/blue overlays show ± 3 unit traversals along each latent dimension while keeping other dimensions fixed. z_1 picks up the biggest source of variation: shorter stride length and stiffer limbs, both hallmarks of hemiplegic gait [Li, 2023]. z_2 is about left arm variability, z_3 combines left arm and right knee variability, z_4 tracks right arm variability, and z_5 captures subtle elbow movement differences.

5.5 Correlation with Clinical Scores in Stroke Dataset

Figure 4 shows correlations between the first five ES-VAE latent dimensions and clinical/demographic variables. Both z_1 and z_3 correlate negatively with POMA ($r = -0.50$ and $r = -0.41$), meaning

Table 2: NTU-60 ten-class classification under subject-wise cross-validation (Leave-5-Subjects-Out, 8 folds, 40 subjects). Metrics are macro-averaged F1-score, precision, and recall. Values are point estimates with raised 95% bootstrap confidence intervals in parentheses.

Input Representation	Method	Macro F1	Macro Precision	Macro Recall
Raw Skeleton	TCN	0.21 ^(0.17–0.25)	0.23 ^(0.18–0.29)	0.23 ^(0.19–0.27)
	LSTM	0.20 ^(0.16–0.23)	0.21 ^(0.16–0.26)	0.22 ^(0.19–0.25)
	Transformer	0.33 ^(0.29–0.38)	0.34 ^(0.28–0.40)	0.36 ^(0.32–0.41)
	ST-GCN	0.11 ^(0.08–0.13)	0.13 ^(0.08–0.18)	0.11 ^(0.09–0.14)
	Sparse ST-GCN	0.49 ^(0.44–0.54)	0.52 ^(0.47–0.57)	0.51 ^(0.46–0.55)
	Hyper-GCN	0.54 ^(0.50–0.58)	0.56 ^(0.52–0.60)	0.55 ^(0.51–0.59)
	PCA + k -NN	0.48 ^(0.44–0.53)	0.55 ^(0.49–0.60)	0.50 ^(0.45–0.54)
	VAE + k -NN	0.27 ^(0.22–0.31)	0.26 ^(0.22–0.31)	0.27 ^(0.23–0.31)
Tangent Vector	TCN	0.39 ^(0.35–0.43)	0.41 ^(0.36–0.47)	0.43 ^(0.39–0.47)
	LSTM	0.38 ^(0.33–0.42)	0.39 ^(0.33–0.47)	0.42 ^(0.38–0.47)
	Transformer	0.44 ^(0.40–0.48)	0.46 ^(0.40–0.53)	0.48 ^(0.44–0.52)
	ST-GCN	0.41 ^(0.37–0.45)	0.41 ^(0.36–0.46)	0.46 ^(0.42–0.50)
	Sparse ST-GCN	0.50 ^(0.46–0.54)	0.50 ^(0.46–0.54)	0.52 ^(0.47–0.56)
	Hyper-GCN	0.38 ^(0.33–0.42)	0.44 ^(0.39–0.49)	0.38 ^(0.33–0.43)
	Tangent PCA + k -NN	0.50 ^(0.45–0.54)	0.54 ^(0.50–0.59)	0.50 ^(0.46–0.55)
	ES-VAE + k-NN (proposed)	0.56 ^(0.52–0.60)	0.57 ^(0.53–0.62)	0.56 ^(0.52–0.61)

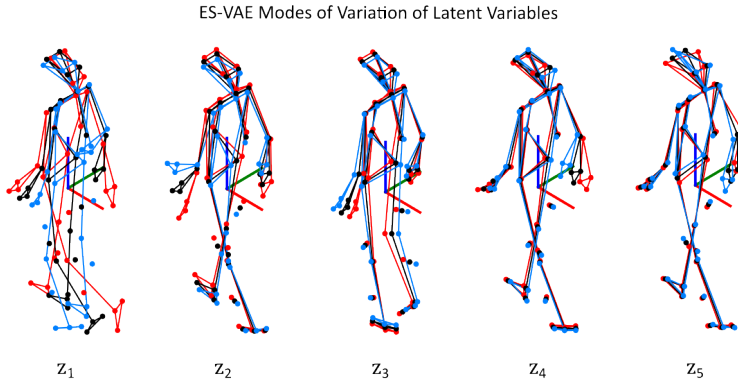


Figure 3: ES-VAE modes of variation: z_1 (short stride and stiffer limbs), z_2 (left arm variability), z_3 (left arm and right knee variability), z_4 (right arm variability), z_5 (subtle right elbow variability). Black: mean; red/blue: ± 3 traversals.

that participants who score higher on z_1 and z_3 (shorter stride, stiffer limbs) also score lower on POMA. z_4 correlates positively with LesionLeft, which shows that it encodes left side disability.

5.6 Ablation Studies

We did different ablation studies to understand the effect of different components of our modeling approach. The ablation studies are described in detail in Appendix Section F.

6 Discussion

Across both datasets, the dominant pattern is that geometry-aware preprocessing matters more than raw model capacity. Once translation, rotation, scale are removed in Kendall shape space and rate variability removed using TSRVF framework, even simple tangent-space baselines become much stronger. ES-VAE improves further by replacing a linear projection with a nonlinear generative

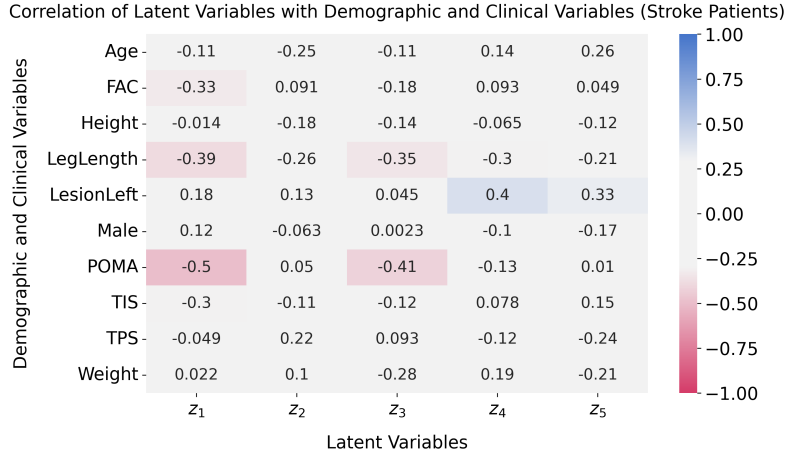


Figure 4: Correlation of demographic and clinical variables with the first five ES-VAE latent dimensions. z_1 and z_3 correlate negatively with POMA, and z_4 correlates with lesion laterality.

model. The analyses show that this gain is not merely predictive: the learned latent dimensions remain interpretable in terms of stride length, limb stiffness, and lateralized arm motion.

The same representation also generalizes across tasks. On stroke gait, it supports clinically meaningful regression and laterality classification; on NTU-60, it improves recognition of actions whose discriminative signal lies in motion shape rather than static pose. This suggests that the main benefit of ES-VAE is structural, namely that it allocates model capacity to shape dynamics after nuisance variability has been removed geometrically.

There are a few clear limitations. The stroke dataset has only $N = 155$ participants and NTU-60 subset contains 40 participants and comes from a single center or lab, so we do not yet know how well the approach generalizes to other populations or motion capture setups. The class imbalance (111 healthy vs. 14 left stroke vs. 30 right stroke) makes laterality classification hard, and the confidence intervals for left-stroke classification are wide. We also kept the encoder-decoder deliberately simple for interpretability. A more expressive architecture (convolutional, attention-based) might push performance further, though probably at the expense of interpretability. Finally, we only use kinematic data. Adding electromyography (EMG) signals could give complementary information about muscle activation patterns.

In future, we plan to scale to larger multi-center datasets, use the model for longitudinal tracking of rehabilitation progress, explore multimodal models incorporating EMG, and conditional VAEs that incorporate participant demographics for personalized activity and gait assessment.

7 Conclusion

We presented ES-VAE, a Riemannian VAE that works on skeleton trajectories in Kendall shape space with transported SRVF temporal alignment, making the representation invariant to translations, rotations, scaling, and activity speed all at once. On a stroke dataset, the model learns a compact latent space where individual dimensions map onto recognizable gait features like stride length reduction, limb stiffness, and lateralized arm variability. It predicts POMA scores with $R^2 = 0.74$ and classifies 10 different activities with macro F1 = 0.56, outperforming other methods. The results show the advantage of removing geometric noise early using shape-space embedding than to expect a deep network to learn those invariances by itself. Additionally, the nonlinear mapping of a ES-VAE gives a more useful decomposition of gait and action variability than linear tangent PCA. These results make ES-VAE a practical option for interpretable, automated skeleton pose trajectory analysis in stroke rehabilitation and activity recognition.

References

- Vida Adeli, Soroush Mehraban, Irene Ballester, Yasamin Zarghami, Andrea Sabo, Andrea Iaboni, and Babak Taati. Benchmarking skeleton-based motion encoder models for clinical applications: Estimating Parkinson’s disease severity in walking sequences. In *2024 IEEE 18th International Conference on Automatic Face and Gesture Recognition (FG)*, pages 1–10. IEEE, 2024.
- Boulbaba Ben Amor, Jingyong Su, and Anuj Srivastava. Action recognition using rate-invariant analysis of skeletal shape trajectories. *IEEE Transactions on Pattern Analysis and Machine Intelligence*, 38(1):1–13, 2016.
- Dimitri Bertsekas. *Dynamic programming and optimal control: Volume I*, volume 4. Athena scientific, 2012.
- Alexandre Bône, Maxime Louis, Olivier Colliot, Stanley Durrleman, and Alzheimer’s Disease Neuroimaging Initiative. Learning low-dimensional representations of shape data sets with diffeomorphic autoencoders. In *Proc. Int. Conf. Information Processing in Medical Imaging (IPMI)*, pages 195–207. Springer, 2019.
- Clément Chadebec and Stéphanie Allasonnière. A geometric perspective on variational autoencoders. *Advances in Neural Information Processing Systems*, 35:19618–19630, 2022.
- Clément Chadebec, Elina Thibeu-Sutre, Ninon Burgos, and Stéphanie Allasonnière. Data augmentation in high dimensional low sample size setting using a geometry-based variational autoencoder. *IEEE Transactions on Pattern Analysis and Machine Intelligence*, 45(3):2879–2896, 2022.
- Jieun Cho, Sunghe Ha, Jooyoung Lee, Minseok Kim, and Hogene Kim. Stroke walking and balance characteristics via principal component analysis. *Scientific Reports*, 14(1):10465, 2024.
- Ian L Dryden and Kanti V Mardia. *Statistical shape analysis: with applications in R*. John Wiley & Sons, 2016.
- Sven Dummer, Christoph Brune, and Nicola Strisciuglio. RSA-INR: Riemannian shape autoencoding via 4D implicit neural representations. Preprint, University of Twente, 2023.
- Sven Dummer, Nicola Strisciuglio, and Christoph Brune. RDA-INR: Riemannian diffeomorphic autoencoding via implicit neural representations. *SIAM Journal on Imaging Sciences*, 17(4): 2302–2330, 2024.
- Nadav Eichler, Hagit Hel-Or, Ilan Shimshoni, Dorit Itah, Bella Gross, and Shmuel Raz. 3D motion capture system for assessing patient motion during Fugl-Meyer stroke rehabilitation testing. *IET Computer Vision*, 12(7):963–975, 2018.
- Chao Fan, Jingzhe Ma, Dongyang Jin, Chuanfu Shen, and Shiqi Yu. SkeletonGait: Gait recognition using skeleton maps. In *Proceedings of the AAAI conference on artificial intelligence*, volume 38, pages 1662–1669, 2024.
- Rasha Friji, Hassen Drira, Faten Chaieb, Hamza Kchok, and Sebastian Kurtek. Geometric deep neural network using rigid and non-rigid transformations for human action recognition. In *Proc. IEEE/CVF Int. Conf. Computer Vision (ICCV)*, pages 12611–12620, 2021.
- Yihang Fu, Lifang He, and Qingyu Chen. ManifoldFormer: Geometric deep learning for neural dynamics on Riemannian manifolds. *arXiv preprint arXiv:2511.16828*, 2025.
- Anthony A Gatti, Louis Blankemeier, Dave Van Veen, Brian Hargreaves, Scott L Delp, Garry E Gold, Feliks Kogan, and Akshay S Chaudhari. ShapeMed-Knee: A dataset and neural shape model benchmark for modeling 3D femurs. *IEEE Transactions on Medical Imaging*, 44(3):1140–1152, 2025.
- Tal Hakim and Ilan Shimshoni. A-MAL: Automatic motion assessment learning from properly performed motions in 3d skeleton videos. In *Proceedings of the IEEE/CVF international conference on computer vision workshops*, pages 0–0, 2019.

- William Harvey, Saeid Naderiparizi, and Frank Wood. Conditional image generation by conditioning variational auto-encoders. In *International Conference on Learning Representations*, 2022. URL <https://openreview.net/forum?id=7MV6uLz0ChW>.
- Sepp Hochreiter and Jürgen Schmidhuber. Long short-term memory. *Neural Computation*, 9(8): 1735–1780, 1997.
- Nadia Hosni, Hassen Drira, Faten Chaieb, and Boulbaba Ben Amor. 3D gait recognition based on functional PCA on Kendall’s shape space. In *Proc. Int. Conf. Pattern Recognition (ICPR)*, pages 2130–2135. IEEE, 2018.
- Dimitris Kalatzis, David Eklund, Georgios Arvanitidis, and Søren Hauberg. Variational autoencoders with riemannian brownian motion priors. *arXiv preprint arXiv:2002.05227*, 2020.
- David G Kendall, Dennis Barden, Thomas K Carne, and Huiling Le. *Shape and Shape Theory*. John Wiley & Sons, 1999.
- Diederik P Kingma and Max Welling. Auto-encoding variational Bayes. *arXiv preprint arXiv:1312.6114*, 2013.
- Colin Lea, Michael D Flynn, Rene Vidal, Austin Reiter, and Gregory D Hager. Temporal convolutional networks for action segmentation and detection. In *Proc. IEEE Conf. Computer Vision and Pattern Recognition (CVPR)*, pages 156–165, 2017.
- Hyun-Seob Lee. Application of dynamic time warping algorithm for pattern similarity of gait. *Journal of Exercise Rehabilitation*, 15(4):526, 2019.
- Sheng Li. Stiff knee gait disorders as neuromechanical consequences of spastic hemiplegia in chronic stroke. *Toxins*, 15(3):204, 2023.
- Romain Lopez, Jeffrey Regier, Michael B Cole, Michael I Jordan, and Nir Yosef. Deep generative modeling for single-cell transcriptomics. *Nature Methods*, 15(12):1053–1058, 2018.
- Nina Miolane and Susan Holmes. Learning weighted submanifolds with variational autoencoders and Riemannian variational autoencoders. In *Proc. IEEE/CVF Conf. Computer Vision and Pattern Recognition (CVPR)*, pages 14503–14511, 2020.
- Nina Miolane, Nicolas Guigui, Alice Le Brigant, Johan Mathe, Benjamin Hou, Yann Thanwerdas, Stefan Heyder, Olivier Peltre, Niklas Koep, Hadi Zaatiti, Hatem Hajri, Yann Cabanes, Thomas Gerald, Paul Chauchat, Christian Shewmake, Daniel Brooks, Bernhard Kainz, Claire Donnat, Susan Holmes, and Xavier Pennec. Geomstats: A python package for riemannian geometry in machine learning. *Journal of Machine Learning Research*, 21(223):1–9, 2020. URL <http://jmlr.org/papers/v21/19-027.html>.
- Amir Shahroudy, Jun Liu, Tian-Tsong Ng, and Gang Wang. NTU RGB+D: A large scale dataset for 3D human activity analysis. In *Proceedings of the IEEE conference on computer vision and pattern recognition*, pages 1010–1019, 2016.
- Pourya Shamsolmoali, Masoumeh Zareapoor, Huiyu Zhou, Dacheng Tao, and Xuelong Li. Vtae: Variational transformer autoencoder with manifolds learning. *IEEE Transactions on Image Processing*, 32:4486–4500, 2023.
- Zehua Sun, Qihong Ke, Hossein Rahmani, Mohammed Bennamoun, Gang Wang, and Jun Liu. Human action recognition from various data modalities: A review. *IEEE transactions on pattern analysis and machine intelligence*, 45(3):3200–3225, 2022.
- Paolo Tormene, Toni Giorgino, Silvana Quaglini, and Mario Stefanelli. Matching incomplete time series with dynamic time warping: an algorithm and an application to post-stroke rehabilitation. *Artificial Intelligence in Medicine*, 45(1):11–34, 2009.
- J Derek Tucker, Wei Wu, and Anuj Srivastava. Generative models for functional data using phase and amplitude separation. *Computational Statistics & Data Analysis*, 61:50–66, 2013.

- Sharvaree Vadgama, Jakub Mikolaj Tomczak, and Erik J Bekkers. Kendall shape-vae: Learning shapes in a generative framework. In *NeurIPS 2022 Workshop on Symmetry and Geometry in Neural Representations*, 2022.
- Tamaya Van Crieking, Wim Saeys, Steven Truijen, Luc Vereeck, Lizeth H Sloot, and Ann Hallemans. A full-body motion capture gait dataset of 138 able-bodied adults across the life span and 50 stroke survivors. *Scientific Data*, 10(1):852, 2023.
- Ashish Vaswani, Noam Shazeer, Niki Parmar, Jakob Uszkoreit, Llion Jones, Aidan N Gomez, Łukasz Kaiser, and Illia Polosukhin. Attention is all you need. In *Advances in Neural Information Processing Systems*, volume 30, 2017.
- Jianyang Xie, Yitian Zhao, Yanda Meng, He Zhao, Anh Nguyen, and Yalin Zheng. Are spatial-temporal graph convolution networks for human action recognition over-parameterized? In *Proceedings of the Computer Vision and Pattern Recognition Conference*, pages 24309–24319, 2025.
- Sijie Yan, Yuanjun Xiong, and Dahua Lin. Spatial temporal graph convolutional networks for skeleton-based action recognition. In *Proc. AAAI Conf. Artificial Intelligence*, volume 32, 2018.
- Zhe Zhang, Qiang Fang, and Xudong Gu. Objective assessment of upper-limb mobility for poststroke rehabilitation. *IEEE Transactions on Biomedical Engineering*, 63(4):859–868, 2016. doi: 10.1109/TBME.2015.2477095.
- Youwei Zhou, Tianyang Xu, Cong Wu, Xiaojun Wu, and Josef Kittler. Adaptive hyper-graph convolution network for skeleton-based human action recognition with virtual connections. In *Proceedings of the IEEE/CVF International Conference on Computer Vision*, pages 12648–12658, 2025.

NeurIPS Paper Checklist

1. Claims

Question: Do the main claims made in the abstract and introduction accurately reflect the paper’s contributions and scope?

Answer: [Yes]

Justification: The abstract and introduction outline the key challenges addressed, our contributions, and a summary of the experimental findings.

Guidelines:

- The answer [N/A] means that the abstract and introduction do not include the claims made in the paper.
- The abstract and/or introduction should clearly state the claims made, including the contributions made in the paper and important assumptions and limitations. A [No] or [N/A] answer to this question will not be perceived well by the reviewers.
- The claims made should match theoretical and experimental results, and reflect how much the results can be expected to generalize to other settings.
- It is fine to include aspirational goals as motivation as long as it is clear that these goals are not attained by the paper.

2. Limitations

Question: Does the paper discuss the limitations of the work performed by the authors?

Answer: [Yes]

Justification: Yes we included the limitations in Section 6.

Guidelines:

- The answer [N/A] means that the paper has no limitation while the answer [No] means that the paper has limitations, but those are not discussed in the paper.
- The authors are encouraged to create a separate “Limitations” section in their paper.
- The paper should point out any strong assumptions and how robust the results are to violations of these assumptions (e.g., independence assumptions, noiseless settings, model well-specification, asymptotic approximations only holding locally). The authors should reflect on how these assumptions might be violated in practice and what the implications would be.
- The authors should reflect on the scope of the claims made, e.g., if the approach was only tested on a few datasets or with a few runs. In general, empirical results often depend on implicit assumptions, which should be articulated.
- The authors should reflect on the factors that influence the performance of the approach. For example, a facial recognition algorithm may perform poorly when image resolution is low or images are taken in low lighting. Or a speech-to-text system might not be used reliably to provide closed captions for online lectures because it fails to handle technical jargon.
- The authors should discuss the computational efficiency of the proposed algorithms and how they scale with dataset size.
- If applicable, the authors should discuss possible limitations of their approach to address problems of privacy and fairness.
- While the authors might fear that complete honesty about limitations might be used by reviewers as grounds for rejection, a worse outcome might be that reviewers discover limitations that aren’t acknowledged in the paper. The authors should use their best judgment and recognize that individual actions in favor of transparency play an important role in developing norms that preserve the integrity of the community. Reviewers will be specifically instructed to not penalize honesty concerning limitations.

3. Theory assumptions and proofs

Question: For each theoretical result, does the paper provide the full set of assumptions and a complete (and correct) proof?

Answer: [N/A]

Justification: The paper does not contain theoretical results.

Guidelines:

- The answer [N/A] means that the paper does not include theoretical results.
- All the theorems, formulas, and proofs in the paper should be numbered and cross-referenced.
- All assumptions should be clearly stated or referenced in the statement of any theorems.
- The proofs can either appear in the main paper or the supplemental material, but if they appear in the supplemental material, the authors are encouraged to provide a short proof sketch to provide intuition.
- Inversely, any informal proof provided in the core of the paper should be complemented by formal proofs provided in appendix or supplemental material.
- Theorems and Lemmas that the proof relies upon should be properly referenced.

4. Experimental result reproducibility

Question: Does the paper fully disclose all the information needed to reproduce the main experimental results of the paper to the extent that it affects the main claims and/or conclusions of the paper (regardless of whether the code and data are provided or not)?

Answer: [Yes]

Justification: We have provided the experimental details in Section 4 and additional experimental details in Appendix Section D to fully to reproduce the results.

Guidelines:

- The answer [N/A] means that the paper does not include experiments.
- If the paper includes experiments, a [No] answer to this question will not be perceived well by the reviewers: Making the paper reproducible is important, regardless of whether the code and data are provided or not.
- If the contribution is a dataset and/or model, the authors should describe the steps taken to make their results reproducible or verifiable.
- Depending on the contribution, reproducibility can be accomplished in various ways. For example, if the contribution is a novel architecture, describing the architecture fully might suffice, or if the contribution is a specific model and empirical evaluation, it may be necessary to either make it possible for others to replicate the model with the same dataset, or provide access to the model. In general, releasing code and data is often one good way to accomplish this, but reproducibility can also be provided via detailed instructions for how to replicate the results, access to a hosted model (e.g., in the case of a large language model), releasing of a model checkpoint, or other means that are appropriate to the research performed.
- While NeurIPS does not require releasing code, the conference does require all submissions to provide some reasonable avenue for reproducibility, which may depend on the nature of the contribution. For example
 - (a) If the contribution is primarily a new algorithm, the paper should make it clear how to reproduce that algorithm.
 - (b) If the contribution is primarily a new model architecture, the paper should describe the architecture clearly and fully.
 - (c) If the contribution is a new model (e.g., a large language model), then there should either be a way to access this model for reproducing the results or a way to reproduce the model (e.g., with an open-source dataset or instructions for how to construct the dataset).
 - (d) We recognize that reproducibility may be tricky in some cases, in which case authors are welcome to describe the particular way they provide for reproducibility. In the case of closed-source models, it may be that access to the model is limited in some way (e.g., to registered users), but it should be possible for other researchers to have some path to reproducing or verifying the results.

5. Open access to data and code

Question: Does the paper provide open access to the data and code, with sufficient instructions to faithfully reproduce the main experimental results, as described in supplemental material?

Answer: [Yes]

Justification: We used two public datasets which were cited properly and we plan to publicly release our code once the status of the paper is confirmed. Additionally we shared the codes with all the instructions in README.md as supplementary files.

Guidelines:

- The answer [N/A] means that paper does not include experiments requiring code.
- Please see the NeurIPS code and data submission guidelines (<https://neurips.cc/public/guides/CodeSubmissionPolicy>) for more details.
- While we encourage the release of code and data, we understand that this might not be possible, so [No] is an acceptable answer. Papers cannot be rejected simply for not including code, unless this is central to the contribution (e.g., for a new open-source benchmark).
- The instructions should contain the exact command and environment needed to run to reproduce the results. See the NeurIPS code and data submission guidelines (<https://neurips.cc/public/guides/CodeSubmissionPolicy>) for more details.
- The authors should provide instructions on data access and preparation, including how to access the raw data, preprocessed data, intermediate data, and generated data, etc.
- The authors should provide scripts to reproduce all experimental results for the new proposed method and baselines. If only a subset of experiments are reproducible, they should state which ones are omitted from the script and why.
- At submission time, to preserve anonymity, the authors should release anonymized versions (if applicable).
- Providing as much information as possible in supplemental material (appended to the paper) is recommended, but including URLs to data and code is permitted.

6. Experimental setting/details

Question: Does the paper specify all the training and test details (e.g., data splits, hyperparameters, how they were chosen, type of optimizer) necessary to understand the results?

Answer: [Yes]

Justification: All the training and test details are given in Appendix Section D.

Guidelines:

- The answer [N/A] means that the paper does not include experiments.
- The experimental setting should be presented in the core of the paper to a level of detail that is necessary to appreciate the results and make sense of them.
- The full details can be provided either with the code, in appendix, or as supplemental material.

7. Experiment statistical significance

Question: Does the paper report error bars suitably and correctly defined or other appropriate information about the statistical significance of the experiments?

Answer: [Yes]

Justification: The results are reported with 95% confidence intervals. Additional details about factors of variability, method for calculating confidence intervals are given Appendix Section D.4.

Guidelines:

- The answer [N/A] means that the paper does not include experiments.
- The authors should answer [Yes] if the results are accompanied by error bars, confidence intervals, or statistical significance tests, at least for the experiments that support the main claims of the paper.
- The factors of variability that the error bars are capturing should be clearly stated (for example, train/test split, initialization, random drawing of some parameter, or overall run with given experimental conditions).
- The method for calculating the error bars should be explained (closed form formula, call to a library function, bootstrap, etc.)

- The assumptions made should be given (e.g., Normally distributed errors).
- It should be clear whether the error bar is the standard deviation or the standard error of the mean.
- It is OK to report 1-sigma error bars, but one should state it. The authors should preferably report a 2-sigma error bar than state that they have a 96% CI, if the hypothesis of Normality of errors is not verified.
- For asymmetric distributions, the authors should be careful not to show in tables or figures symmetric error bars that would yield results that are out of range (e.g., negative error rates).
- If error bars are reported in tables or plots, the authors should explain in the text how they were calculated and reference the corresponding figures or tables in the text.

8. Experiments compute resources

Question: For each experiment, does the paper provide sufficient information on the computer resources (type of compute workers, memory, time of execution) needed to reproduce the experiments?

Answer: [Yes]

Justification: All the information on compute resources are given in Appendix Section D.6.

Guidelines:

- The answer [N/A] means that the paper does not include experiments.
- The paper should indicate the type of compute workers CPU or GPU, internal cluster, or cloud provider, including relevant memory and storage.
- The paper should provide the amount of compute required for each of the individual experimental runs as well as estimate the total compute.
- The paper should disclose whether the full research project required more compute than the experiments reported in the paper (e.g., preliminary or failed experiments that didn't make it into the paper).

9. Code of ethics

Question: Does the research conducted in the paper conform, in every respect, with the NeurIPS Code of Ethics [https://neurips.cc/public/EthicsGuidelines?](https://neurips.cc/public/EthicsGuidelines)

Answer: [Yes]

Justification: The research fully follows the NeurIPS Code of Ethics.

Guidelines:

- The answer [N/A] means that the authors have not reviewed the NeurIPS Code of Ethics.
- If the authors answer [No], they should explain the special circumstances that require a deviation from the Code of Ethics.
- The authors should make sure to preserve anonymity (e.g., if there is a special consideration due to laws or regulations in their jurisdiction).

10. Broader impacts

Question: Does the paper discuss both potential positive societal impacts and negative societal impacts of the work performed?

Answer: [Yes]

Justification: The broader impact is given in Appendix Section G.

Guidelines:

- The answer [N/A] means that there is no societal impact of the work performed.
- If the authors answer [N/A] or [No], they should explain why their work has no societal impact or why the paper does not address societal impact.
- Examples of negative societal impacts include potential malicious or unintended uses (e.g., disinformation, generating fake profiles, surveillance), fairness considerations (e.g., deployment of technologies that could make decisions that unfairly impact specific groups), privacy considerations, and security considerations.

- The conference expects that many papers will be foundational research and not tied to particular applications, let alone deployments. However, if there is a direct path to any negative applications, the authors should point it out. For example, it is legitimate to point out that an improvement in the quality of generative models could be used to generate Deepfakes for disinformation. On the other hand, it is not needed to point out that a generic algorithm for optimizing neural networks could enable people to train models that generate Deepfakes faster.
- The authors should consider possible harms that could arise when the technology is being used as intended and functioning correctly, harms that could arise when the technology is being used as intended but gives incorrect results, and harms following from (intentional or unintentional) misuse of the technology.
- If there are negative societal impacts, the authors could also discuss possible mitigation strategies (e.g., gated release of models, providing defenses in addition to attacks, mechanisms for monitoring misuse, mechanisms to monitor how a system learns from feedback over time, improving the efficiency and accessibility of ML).

11. Safeguards

Question: Does the paper describe safeguards that have been put in place for responsible release of data or models that have a high risk for misuse (e.g., pre-trained language models, image generators, or scraped datasets)?

Answer: [N/A]

Justification: The paper does not have such risks.

Guidelines:

- The answer [N/A] means that the paper poses no such risks.
- Released models that have a high risk for misuse or dual-use should be released with necessary safeguards to allow for controlled use of the model, for example by requiring that users adhere to usage guidelines or restrictions to access the model or implementing safety filters.
- Datasets that have been scraped from the Internet could pose safety risks. The authors should describe how they avoided releasing unsafe images.
- We recognize that providing effective safeguards is challenging, and many papers do not require this, but we encourage authors to take this into account and make a best faith effort.

12. Licenses for existing assets

Question: Are the creators or original owners of assets (e.g., code, data, models), used in the paper, properly credited and are the license and terms of use explicitly mentioned and properly respected?

Answer: [Yes]

Justification: The original owners of assets (e.g., data, models) are properly cited and credited. The stroke dataset is cited to its original Figshare/Springer Nature record and used under the dataset's CC0 license. The NTU RGB+D dataset is credited to the ROSE Lab at Nanyang Technological University and cited using the required dataset paper; we follow its terms of use for academic, non-commercial research and do not redistribute the dataset or the curated subset used in our experiments.

Guidelines:

- The answer [N/A] means that the paper does not use existing assets.
- The authors should cite the original paper that produced the code package or dataset.
- The authors should state which version of the asset is used and, if possible, include a URL.
- The name of the license (e.g., CC-BY 4.0) should be included for each asset.
- For scraped data from a particular source (e.g., website), the copyright and terms of service of that source should be provided.
- If assets are released, the license, copyright information, and terms of use in the package should be provided. For popular datasets, paperswithcode.com/datasets

has curated licenses for some datasets. Their licensing guide can help determine the license of a dataset.

- For existing datasets that are re-packaged, both the original license and the license of the derived asset (if it has changed) should be provided.
- If this information is not available online, the authors are encouraged to reach out to the asset's creators.

13. **New assets**

Question: Are new assets introduced in the paper well documented and is the documentation provided alongside the assets?

Answer: [N/A]

Justification: Currently there are no new assets. We will publicly share the code after the confirmation of the status of the paper. Additionally we shared the codes with all the instructions in README.md as supplementary files.

Guidelines:

- The answer [N/A] means that the paper does not release new assets.
- Researchers should communicate the details of the dataset/code/model as part of their submissions via structured templates. This includes details about training, license, limitations, etc.
- The paper should discuss whether and how consent was obtained from people whose asset is used.
- At submission time, remember to anonymize your assets (if applicable). You can either create an anonymized URL or include an anonymized zip file.

14. **Crowdsourcing and research with human subjects**

Question: For crowdsourcing experiments and research with human subjects, does the paper include the full text of instructions given to participants and screenshots, if applicable, as well as details about compensation (if any)?

Answer: [N/A]

Justification: Crowdsourcing experiments are not done in this paper and the full text of instructions given to participants are available in the original dataset papers that are cited in our papers.

Guidelines:

- The answer [N/A] means that the paper does not involve crowdsourcing nor research with human subjects.
- Including this information in the supplemental material is fine, but if the main contribution of the paper involves human subjects, then as much detail as possible should be included in the main paper.
- According to the NeurIPS Code of Ethics, workers involved in data collection, curation, or other labor should be paid at least the minimum wage in the country of the data collector.

15. **Institutional review board (IRB) approvals or equivalent for research with human subjects**

Question: Does the paper describe potential risks incurred by study participants, whether such risks were disclosed to the subjects, and whether Institutional Review Board (IRB) approvals (or an equivalent approval/review based on the requirements of your country or institution) were obtained?

Answer: [N/A]

Justification: The potential risks incurred by study participants, whether such risks were disclosed to the subjects, and Institutional Review Board (IRB) approvals are available in the original dataset papers that are cited in our papers.

Guidelines:

- The answer [N/A] means that the paper does not involve crowdsourcing nor research with human subjects.

- Depending on the country in which research is conducted, IRB approval (or equivalent) may be required for any human subjects research. If you obtained IRB approval, you should clearly state this in the paper.
- We recognize that the procedures for this may vary significantly between institutions and locations, and we expect authors to adhere to the NeurIPS Code of Ethics and the guidelines for their institution.
- For initial submissions, do not include any information that would break anonymity (if applicable), such as the institution conducting the review.

16. Declaration of LLM usage

Question: Does the paper describe the usage of LLMs if it is an important, original, or non-standard component of the core methods in this research? Note that if the LLM is used only for writing, editing, or formatting purposes and does *not* impact the core methodology, scientific rigor, or originality of the research, declaration is not required.

Answer: [N/A]

Justification: LLM was not used as an important, original, or non-standard component of the core methods in this research and used only for writing, editing, or formatting purposes.

Guidelines:

- The answer [N/A] means that the core method development in this research does not involve LLMs as any important, original, or non-standard components.
- Please refer to our LLM policy in the NeurIPS handbook for what should or should not be described.

A Additional Related Literature

Variational Autoencoders: The variational autoencoder [Kingma and Welling, 2013] jointly trains an encoder that approximates the posterior and a decoder that reconstructs the data, optimizing the evidence lower bound (ELBO). Kingma and Welling showed that the resulting latent dimensions can pick up meaningful factors like facial orientation and expression. Lopez et al. [2018] applied the same idea to single-cell transcriptomics (scVI) and found that VAE codes outperform PCA on clustering, imputation, and differential expression. The nonlinear mapping evidently captures structure that linear methods miss, which is what motivates our extension to shape-space data. Chadebec et al. [2022] proposed a geometry-aware VAE whose latent space is modeled as a Riemannian manifold, enabling it to generate meaningful samples from small datasets. Their method was useful for data augmentation in a medical imaging classification task. Shamsolmoali et al. [2023] introduced a variational spatial-transformer autoencoder that minimizes geodesic distance on Riemannian manifold and it uses geodesic interpolation for better latent representation, reconstruction, image interpolation. Kalatzis et al. [2020] argued that the standard Gaussian prior and Euclidean assumptions in VAEs can lead to poor performance, and proposed a Riemannian Brownian motion prior that provides the latent space with a Riemannian structure, significantly improving the model’s representational capacity. In most of these works, the latent space is modeled as a Riemannian manifold. In contrast, our approach represents the skeleton input in Kendall shape space, which is itself a Riemannian manifold.

Stroke Gait Assessment: On the clinical side, dynamic time warping (DTW) has been used traditionally for comparing gait patterns. Tormene et al. [2009] matched incomplete rehabilitation time series with DTW, Lee [2019] validated it for gait pattern similarity, and Zhang et al. [2016] used DTW distance to measure upper-limb mobility post-stroke. Eichler et al. [2018] built a 3D motion capture system that registers skeletons rotationally via singular value decomposition (SVD) for Fugl-Meyer assessment. Joint angle PCA [Cho et al., 2024] takes a different route, computing principal components of joint angle time series. Li [2023] characterized stiff knee gait as a neuromechanical consequence of spastic hemiplegia. The trouble with DTW is that it is not a proper metric and ignores rotation and scaling. Joint angle PCA, on the other hand, throws away the full 3D spatial information. Working in Kendall shape space avoids both problems because it gives a proper Riemannian metric that is invariant to all of these nuisance transformations.

B Derivation of the Riemannian ELBO

We provide a detailed derivation of the loss function used to train ES-VAE.

B.1 Evidence Lower Bound

Starting from Bayes’ rule:

$$p(z | x) = \frac{p(x | z) p(z)}{p(x)}, \tag{13}$$

we take logarithms and rearrange:

$$\ln p(x) = \ln p(x | z) - \ln p(z | x) + \ln p(z). \tag{14}$$

Introducing the variational approximation $q(z | x)$ by adding and subtracting $\ln q(z | x)$, then taking the expectation under $q(z | x)$:

$$\begin{aligned} \ln p(x) &= \underbrace{\mathbb{E}_{q(z|x)}[\ln p(x|z)] - \text{KL}(q(z|x)||p(z))}_{\text{ELBO}} \\ &\quad + \underbrace{\text{KL}(q(z|x)||p(z|x))}_{\geq 0}. \end{aligned} \tag{15}$$

Since the KL divergence is non-negative, the ELBO is a lower bound on $\ln p(x)$, and maximizing the ELBO is equivalent to minimizing the KL divergence between q and the true posterior.

B.2 KL Divergence for Gaussian Prior

For the standard normal prior $p(z) = \mathcal{N}(\mathbf{0}, \mathbf{I})$ and a diagonal Gaussian encoder $q_\phi(z | v) = \mathcal{N}(\mu(v), \text{diag}(\sigma^2(v)))$ with L latent dimensions:

$$\text{KL}_n = \frac{1}{2} \sum_{j=1}^L (\sigma_j^2(v_n) + \mu_j^2(v_n) - 1 - \log \sigma_j^2(v_n)). \quad (16)$$

For a mini-batch of N samples: $\text{KL} = \frac{1}{N} \sum_{n=1}^N \text{KL}_n$.

B.3 Riemannian Reconstruction Loss

For data on a Riemannian manifold \mathcal{M} , the reconstruction term replaces Euclidean distance with the squared geodesic distance. For a trajectory with T time steps:

$$\text{Recon}_n = \sum_{t=1}^T d_{\Sigma_m^k}(\tilde{\beta}_n(t), \hat{\beta}_n(t))^2, \quad (17)$$

where $d_{\Sigma_m^k}$ is the geodesic distance on the shape manifold, $\tilde{\beta}_n(t)$ is the input, and $\hat{\beta}_n(t) = \text{Exp}_\mu(f_\theta(z_n))(t)$ is the reconstruction.

B.4 Total Loss

The total loss to minimize (negative ELBO) over a mini-batch:

$$\begin{aligned} \mathcal{L} &= \frac{1}{N} \sum_{n=1}^N (\text{Recon}_n + \beta_{\text{KL}} \cdot \text{KL}_n) \\ &= \frac{1}{N} \sum_{n=1}^N \left(\sum_{t=1}^T d_{\Sigma_m^k}(\tilde{\beta}_n(t), \hat{\beta}_n(t))^2 + \frac{\beta_{\text{KL}}}{2} \sum_{j=1}^L (\sigma_j^2 + \mu_j^2 - 1 - \log \sigma_j^2) \right), \end{aligned}$$

where β_{KL} weights the KL term relative to reconstruction.

C Dataset Details

C.1 Stroke Gait Dataset

We use the publicly available full-body motion capture gait dataset of Van Crielinge et al. [2023], which contains 138 able-bodied adults and 50 stroke survivors. After excluding participants with incomplete recordings, our analysis includes $N = 155$ participants: 111 healthy controls and 44 stroke patients (14 with left-sided and 30 with right-sided hemiplegia). Each participant performed overground walking at a self-selected speed while $k = 32$ reflective markers were tracked by an optical motion capture system, recording $m = 3$ spatial coordinates per marker. Gait cycles were segmented and resampled to $T = 200$ time steps, yielding trajectories of dimension $k \times m \times T = 32 \times 3 \times 200 = 19,200$ per participant. Clinical assessments include the Performance Oriented Mobility Assessment (POMA), Functional Ambulation Category (FAC), and lesion laterality (left or right hemiplegia).

C.2 NTU-60 Action Recognition Subset

To test whether the manifold prior generalizes beyond clinical gait data, we evaluate the same Kendall shape-space pipeline on a curated subset of the NTU RGB+D (NTU-60) dataset [Shahroudy et al., 2016]. We use 400 single-person trials drawn from 40 NTU-60 subjects and ten action classes, six of which are deliberately confusable hand-to-face motions (drink water, eat meal, brush teeth, brush hair, phone call, play with phone) and four of which are whole-body anchors (sitting down, standing up, hand waving, pointing). The subset is intentionally adversarial: the hand-to-face classes share a standing-upright posture and one-arm-raised geometry, so absolute pose offers little discriminative

signal and trajectory shape becomes the dominant cue. Each trial is a sequence of $k = 25$ skeleton joints with $m = 3$ spatial coordinates, linearly interpolated to $T = 100$ time steps, yielding tensors of dimension $25 \times 3 \times 100 = 7,500$ per trial. Curation is deterministic given a seed: for each (subject, class) pair, one trial is drawn uniformly across all available (camera, replication) combinations so that the final 400-trial subset spans all 17 NTU-60 setups, all three cameras, and both replications.

D Additional Implementation Details

D.1 Network Architecture

The encoder is a linear layer mapping the D -dimensional tangent vector to a hidden layer of size H , followed by tanh activation and dropout ($p = 0.1$), then two parallel linear heads producing the mean $\mu_\phi \in \mathbb{R}^L$ and log-variance $\log \sigma_\phi^2 \in \mathbb{R}^L$, where L is the latent dimension. The decoder consists of two linear layers ($L \rightarrow H' \rightarrow D$) with tanh activation in between. Latent samples are obtained via the reparameterization trick: $z = \mu_\phi + \sigma_\phi \odot \epsilon$, $\epsilon \sim \mathcal{N}(\mathbf{0}, \mathbf{I})$. The dataset-specific widths are:

Stroke dataset. Tangent vector dimension $D = 32 \times 3 \times 200 = 19,200$, hidden width $H = 128$, decoder hidden $H' = 16$, latent dimension $L = 38$. The hyperparameters (L, H) were selected by a grid search using loss on the validation folds where $L \in \{16, 24, 32, 38, 48, 64\}$, and $H \in \{8, 16, 32, 64, 128, 256\}$.

NTU-60 dataset. Tangent vector dimension $D = 25 \times 3 \times 100 = 7500$, hidden width $H = 768$, decoder hidden $H' = H$, latent dimension $L = 48$. The hyperparameters (L, H) were selected by a grid search using loss on the validation folds where $L \in \{16, 24, 32, 48, 64\}$, and $H \in \{512, 768\}$.

D.2 Training

Models are trained with the Adam optimizer at learning rate 10^{-3} on the ELBO with squared geodesic reconstruction loss and a Gaussian KL prior weighted by β_{kl} . The matched-architecture Vanilla VAE used for the comparison shares R , H , batch size, epochs, and optimizer settings with ES-VAE; only the reconstruction loss differs (Euclidean MSE on raw coordinates vs. squared geodesic distance on Kendall shape space). The KL weight β_{kl} was selected using grid search: $\beta_{\text{kl}} \in \{2^{-5}, 2^{-4}, 2^{-3}, 2^{-2}, 2^{-1}\}$ for the stroke dataset and $\beta_{\text{kl}} \in \{10^{-5}, 10^{-4}, 10^{-3}, 10^{-2}, 10^{-1}\}$ for the NTU-60 dataset. For NTU-60, the final ES-VAE used 150 epochs, batch size 64, and $\beta = 10^{-4}$. For the stroke dataset, the final ES-VAE used 100 epochs, full-batch training, and $\beta_{\text{kl}} = 2^{-3}$.

D.3 Inference

After training, latent dimensions are reordered by decreasing variance across the dataset so that z_1 captures the largest source of variation. Downstream prediction uses k -nearest-neighbour retrieval in the latent space with inverse-distance weighting, using the scikit-learn default of $k = 5$ on both datasets. Test sequences are encoded with the trained encoder and matched against the training-fold latent codes.

D.4 Evaluation Protocol

Stroke dataset. All metrics are computed from pooled out-of-fold test predictions under subject-wise cross-validation with 30 folds: 28 folds arranged as two rounds of 14 folds, each with 5 validation and 5 test participants; one fold with 10 validation and 5 test participants; and one fold with 5 validation and 10 test participants. Standardization and Fréchet mean fitted on the training set of each fold. Confidence intervals are obtained via subject-level bootstrap resampling (2000 replicates).

NTU-60 dataset. We evaluate under cross-subject leave-five-subjects-out cross-validation: the 40 subjects are partitioned into 8 disjoint blocks of 5 where each fold trains on 30 subjects, validates on different 5, and tests on the different held-out 5. Standardization and Fréchet mean are refit on each training fold. Macro-averaged F1, precision, and recall are reported with 95% confidence intervals from subject-level bootstrap resampling (2000 replicates).

D.5 Baseline Architectures and Compute Parity

Because the training set is small (300 samples per fold for NTU-60 top10 L5SO, and ≈ 145 for the stroke 30-fold split), every deep baseline is deliberately under-parameterized so that capacity is matched, not maximized. All sequence baselines (TCN, LSTM, Transformer, ST-GCN) share the same training procedure as ES-VAE.

NTU-60 sequence baselines. All four models are trained for 150 epochs at learning rate 2×10^{-3} , weight decay 10^{-4} , batch size 64, and label smoothing 0.05 on cross-entropy. (i) *TCN*: two residual temporal blocks with 16 channels each, kernel size 3, dilations $\{1, 2\}$, BatchNorm + GELU + weight-norm convolutions, dropout 0.40; the head concatenates global-mean and global-max pooled features and applies a 2-layer MLP of width 24 to the 10-class logits. (ii) *LSTM*: a single unidirectional layer with hidden size 16, dropout 0.40, mean+max pooled over time, and the same 2-layer head. (iii) *Transformer*: a 1-layer pre-norm encoder with $d_{\text{model}} = 24$, 2 heads, $d_{\text{ff}} = 48$, dropout 0.30, sinusoidal positional encoding, and mean pooling. (iv) *ST-GCN*: a 2-block spatio-temporal GCN with channel widths (16, 32), temporal kernel 9, dropout 0.30, NTU-25 kinematic adjacency with symmetric normalization, and global average pooling over time and joints. Total trainable parameters are well under 50k for every sequence baseline, deliberately keeping their capacity comparable to the ES-VAE encoder.

NTU-60 official graph baselines (Hyper-GCN, Sparse-ST-GCN). Both graph baselines are run from unmodified architecture code copied from the official releases. Only the data adapter (10-class loader, our 8-fold L5SO split) and the lightweight training harness are local. Hyper-GCN uses the published variant with 25 joints, `hyper_joints = 3`, the NTU-RGB+D graph in `virtual_ensemble` mode, SGD with Nesterov momentum 0.9, base learning rate 0.05, weight decay 4×10^{-4} , label smoothing 0.1, the official 5-epoch warm-up + step decay at epochs [110, 120], the divergence loss on virtual hyper-joints, and a clip window of 64 frames. Sparse-ST-GCN uses the published 10-block ST-GCN backbone with `sparse_ratio = 0.6` on score-modulated convolutions, base channels 64 with two inflations at blocks 5 and 8 (giving $64 \rightarrow 128 \rightarrow 256$), SGD with Nesterov momentum 0.9, base learning rate 0.1 with cosine schedule, weight decay 5×10^{-4} , batch size 32, clip length 60, and a sparse-warm-up phase set to 60% of training. Both runs use 150 epochs, the same 8-fold L5SO partition, deterministic seed 42, and `label_smoothing=0.1`; on the raw-skeleton stream we apply the official joint-modality center-trajectory transform and `random_rot` augmentation, while the tangent-vector stream disables both (the data are already centered and rotation-aligned). We deliberately did not retune any of these official hyperparameters for the small-data regime: the goal of including them is to expose, not erase, the overfitting characteristic of full-capacity NTU graph backbones at 300 training samples.

Stroke gait baselines. Each subject is encoded as a tangent-vector array of shape (32, 3, 200) (or the matched raw-marker tensor of the same shape). All sequence baselines slide a window of size 100 with stride 25 across the temporal axis (5 windows per trial), train on per-window targets with subject-level WeightedRandomSampler ($1/\sqrt{n_c}$ class weights) for the 3-class classifier, and aggregate window predictions per subject by median (regression) or softmax averaging followed by argmax (classification). All four sequence models share Adam with learning rate 5×10^{-4} , weight decay 10^{-4} , batch size 32, cosine annealing, gradient clipping 1.0, SmoothL1 loss for regression, and cross-entropy for classification. The matched per-model widths are: (i) *TCN*, 140 regression epochs / 160 classification epochs): three temporal blocks, channels (64, 64, 96) for regression and (32, 32) for classification, kernel size 5, dropout 0.25/0.35, head hidden width 64/32. (ii) *LSTM*: 1 layer, hidden 64 (regression) or 32 (classification), dropout 0.15, unidirectional, last-step + projection head. (iii) *Transformer*: 1 encoder layer, $d_{\text{model}} = 24$, $d_{\text{ff}} = 64$, 2 heads, dropout 0.10 (regression); $d_{\text{model}} = 12$, $d_{\text{ff}} = 32$, 2 heads, dropout 0.20 (classification). (iv) *ST-GCN*: a 32-node skeleton graph with the symmetric-normalized adjacency, two ST blocks with channel widths (32, 64) for regression and (16, 32) for classification, temporal kernel 7, dropout 0.20/0.30. The default training horizons for the LSTM/Transformer/ST-GCN classifier and regressor are 6 and 8 epochs respectively (the small-window-multiplied effective batch count is large), while TCN trains substantially longer because its much higher capacity needs more updates to reach plateau on the same ≈ 145 -subject training fold. Stroke graph baselines (Hyper-GCN, Sparse-ST-GCN) reuse the unmodified official architectures with the same regression/classification head adaptations as in the NTU runs and identical optimizer/schedule defaults.

Compute parity statement. For every dataset and every CV fold, all baselines and ES-VAE see (a) identical training/test indices, (b) identical preprocessing (per-channel z -score, identical windowing where applicable), (c) the same deterministic seed, and (d) the same evaluation pipeline (pooled out-of-fold predictions with 2000-iteration subject-level bootstrap CIs). All the models were tuned to achieve their best performance.

D.6 Compute Resources

All experiments were run on a single workstation with two Intel Xeon Silver 4210R CPUs (20 cores / 40 threads, 2.40 GHz), 128 GB RAM, and one NVIDIA RTX A5000 GPU (24 GB VRAM), running CUDA 11.8 with PyTorch 2.5.1. We used FDASRSF [Tucker et al., 2013] and Geomstats [Miolane et al., 2020] packages for shape alignment. No multi-GPU or cluster compute was used.

E Additional Results

E.1 Mean Shapes in Stroke Dataset

The mean gait cycles computed from registered trajectories are shown in Figure 5. Stroke patients (red) exhibit characteristic hemiplegic dragging, reduced stride length, and stiffer limb motion compared to the fluid, symmetric gait of healthy subjects (blue).

E.2 Classification Performance on Stroke Dataset

Table 3 gives the three-class classification results (Healthy vs. Left Stroke vs. Right Stroke). ES-VAE leads with a macro F1 of 0.83. Raw-skeleton deep learning methods lag well behind: LSTM gets 0.56, TCN 0.64, Transformer 0.63. The fact that tangent-vector methods (Tangent PCA 0.79, ES-VAE 0.83) do so much better than raw-skeleton methods really underlines how much removing geometric confounders matters.

Table 3: Three-class classification performance for Healthy vs. Left Stroke vs. Right Stroke. Metrics are macro-averaged F1-score, precision, and recall under subject-wise cross-validation. Values are point estimates with raised 95% bootstrap confidence intervals in parentheses.

Input Representation	Method	Macro F1	Macro Precision	Macro Recall
Raw Skeleton	TCN	0.64 ^(0.53–0.72)	0.70 ^(0.53–0.87)	0.62 ^(0.54–0.69)
	LSTM	0.56 ^(0.48–0.63)	0.57 ^(0.47–0.67)	0.56 ^(0.49–0.62)
	Transformer	0.63 ^(0.54–0.70)	0.63 ^(0.54–0.72)	0.63 ^(0.54–0.72)
	ST-GCN	0.39 ^(0.33–0.44)	0.48 ^(0.38–0.59)	0.40 ^(0.36–0.44)
	Sparse ST-GCN	0.48 ^(0.40–0.55)	0.75 ^(0.65–0.83)	0.49 ^(0.43–0.56)
	Hyper-GCN	0.47 ^(0.41–0.54)	0.48 ^(0.41–0.55)	0.47 ^(0.40–0.54)
	PCA + k -NN	0.55 ^(0.46–0.62)	0.55 ^(0.46–0.64)	0.55 ^(0.47–0.63)
	VAE + k -NN	0.61 ^(0.51–0.69)	0.68 ^(0.51–0.85)	0.58 ^(0.51–0.67)
Joint Angle	PCA + k -NN	0.61 ^(0.50–0.70)	0.78 ^(0.53–0.90)	0.57 ^(0.49–0.64)
	VAE + k -NN	0.69 ^(0.60–0.78)	0.78 ^(0.66–0.89)	0.65 ^(0.57–0.74)
Tangent Vector	TCN	0.75 ^(0.66–0.83)	0.78 ^(0.68–0.89)	0.74 ^(0.66–0.83)
	LSTM	0.70 ^(0.60–0.79)	0.81 ^(0.69–0.91)	0.67 ^(0.59–0.75)
	Transformer	0.63 ^(0.51–0.71)	0.75 ^(0.51–0.87)	0.60 ^(0.52–0.67)
	ST-GCN	0.48 ^(0.42–0.52)	0.50 ^(0.44–0.56)	0.48 ^(0.43–0.53)
	Sparse ST-GCN	0.53 ^(0.43–0.62)	0.73 ^(0.62–0.85)	0.49 ^(0.44–0.55)
	Hyper-GCN	0.56 ^(0.50–0.62)	0.56 ^(0.49–0.63)	0.57 ^(0.51–0.63)
	Tangent PCA + k -NN	0.79 ^(0.70–0.87)	0.83 ^(0.75–0.92)	0.76 ^(0.68–0.85)
ES-VAE + k-NN (proposed)	0.83 ^(0.75–0.90)	0.86 ^(0.79–0.93)	0.80 ^(0.73–0.89)	

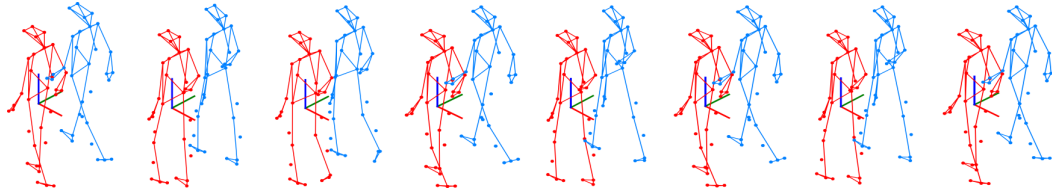


Figure 5: Mean gait cycles from registered trajectories. Stroke patients (red) exhibit hemiplegic dragging, shorter stride length, and stiffer limb motion compared to healthy subjects (blue).

Table 4: Per-class classification report for ES-VAE + k -NN.

Class	Precision	Recall	F1
Stroke (Left)	0.71	0.71	0.72
Stroke (Right)	0.91	0.70	0.79
Healthy	0.94	1.00	0.97
Accuracy			0.92
Macro Avg	0.86	0.80	0.83
Weighted Avg	0.91	0.92	0.91

Looking at the per-class breakdown in Table 4, ES-VAE identifies healthy subjects almost perfectly (F1 = 0.97, recall = 1.00). Separating left from right stroke is harder, but the model still does well: F1 = 0.71 for left stroke, F1 = 0.79 for right stroke, and 0.92 overall accuracy.

E.3 Per-class Classification Report of NTU-60 Dataset

Table 5 breaks the ES-VAE result down by class. The four whole-body anchor classes (sitting down, standing up, hand waving, pointing to something) reach an average F1 of 0.79, while the six hand-to-face classes (drink water, eat meal, brush teeth, brush hair, phone call, play with phone) land at an average F1 of 0.40. The spread is by design: the anchor classes are easy because absolute pose alone discriminates them, whereas the hand-to-face classes share a standing-upright posture and one-arm-raised geometry, so trajectory shape is the only signal available and the manifold prior is most useful there.

Table 5: Per-class classification report for ES-VAE + k -NN on the NTU-60 ten-class subset under leave-five-subjects-out cross-validation.

Class	Precision	Recall	F1
A001 drink water	0.39	0.40	0.40
A002 eat meal	0.44	0.30	0.36
A003 brush teeth	0.32	0.45	0.37
A004 brush hair	0.42	0.33	0.37
A028 phone call	0.42	0.25	0.31
A029 play with phone	0.48	0.80	0.60
A008 sitting down	0.74	0.88	0.80
A009 standing up	0.97	0.80	0.88
A023 hand waving	0.74	0.62	0.68
A031 pointing to something	0.82	0.80	0.81
Accuracy			0.56
Macro Avg	0.57	0.56	0.56
Weighted Avg	0.57	0.56	0.56

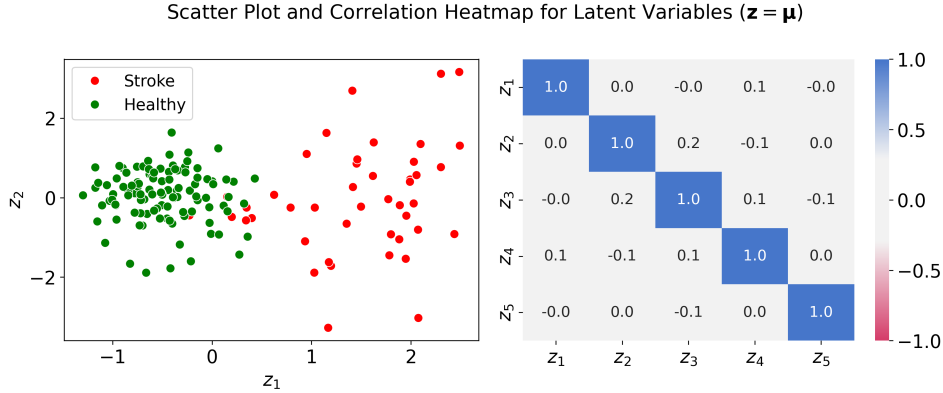


Figure 6: Left: Scatter plot of z_1 vs. z_2 showing separation between stroke (red) and healthy (green) cohorts. Right: Correlation heatmap of the first five latent dimensions, confirming their independence.

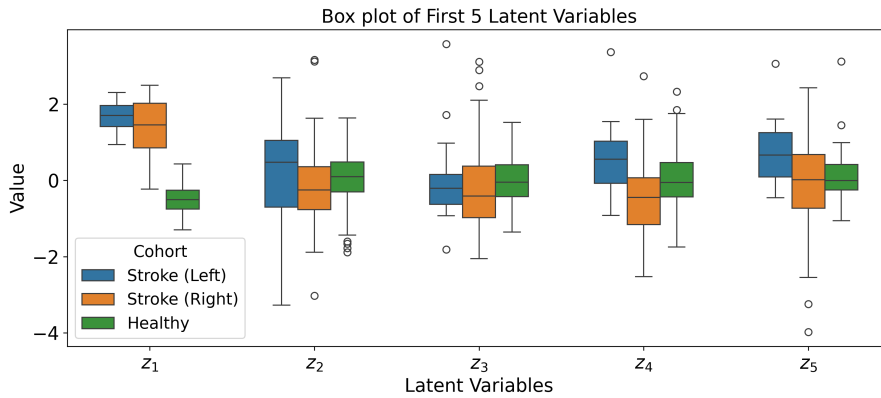


Figure 7: Boxplots of the first five latent dimensions by clinical group. z_1 gives the widest separation between Stroke and Healthy, and z_4 best separates Left from Right hemiplegia.

E.4 Independence and Separability of Latent Variables in Stroke Dataset

Figure 6 shows a scatter plot of z_1 versus z_2 together with a correlation heatmap of the first five latent dimensions. The heatmap shows that the latent variables are largely uncorrelated, so each dimension really is picking up different aspects of gait. In the scatter plot, healthy participants cluster tightly near the origin while stroke patients spread out much more, which fits with how variable post-stroke gait tends to be.

Figure 7 breaks this down further with boxplots by clinical group. z_1 gives the widest gap between Stroke and Healthy, as expected from its link to stride length and limb stiffness. z_4 is the most useful for telling Left from Right stroke apart, consistent with it encoding unilateral arm variability.

E.5 Correlation with Clinical Scores and Tangent PCA in Stroke Dataset

Figure 8 shows that only PC1 reaches $r = 0.50$ with POMA and PC4 shows -0.49 with LesionLeft. So ES-VAE spreads the clinical information over more than one latent dimension (z_1 and z_3 both carry POMA signal), which may give a richer picture than Tangent PCA’s single-dimension correlations.

E.6 Tangent PCA Modes of Variation in Stroke Dataset

Figure 9 shows the first five Tangent PCA modes. PC1 looks a lot like z_1 (stride/stiffness), but the higher modes diverge. PC2 mixes both arms together, while ES-VAE’s z_2 isolates the left arm. PC3 in Tangent PCA blends left arm with some right arm variability, whereas ES-VAE’s z_3 pairs the left

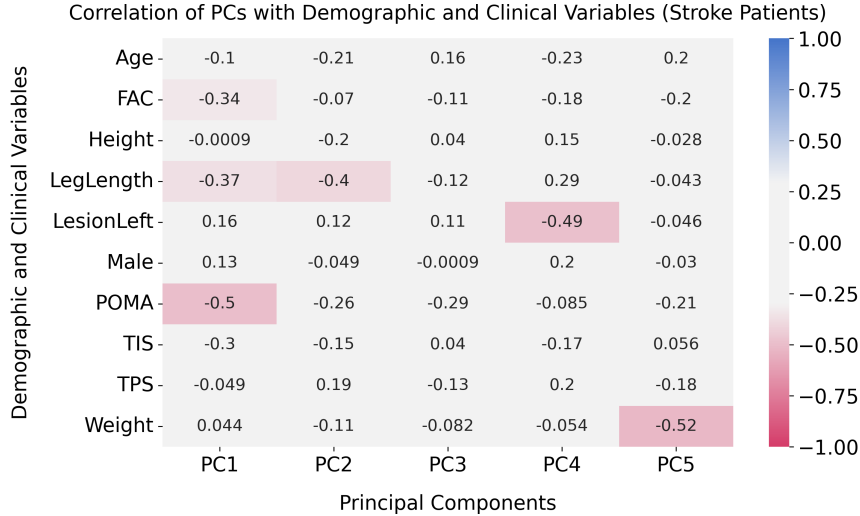


Figure 8: Correlation of demographic and clinical variables with the first five Tangent PCA dimensions.

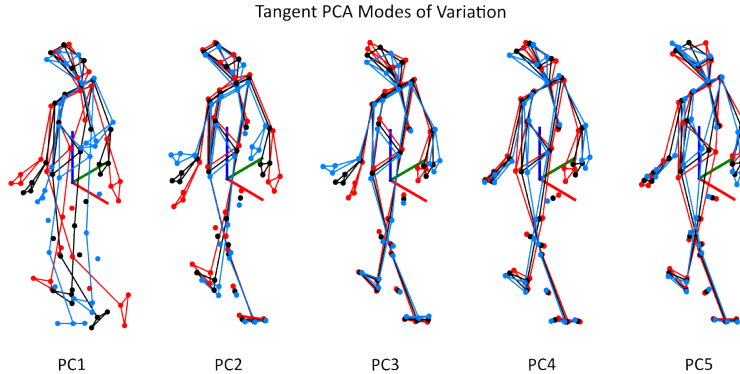


Figure 9: Tangent PCA modes of variation: PC1 (stride/stiffness), PC2 (bilateral arm variability), PC3 (left arm with some right arm), PC4 (right arm with small left hip), PC5 (right hip variability). Black: mean; red/blue: ± 3 traversals.

arm with the right knee. PC5 picks up right hip variability, while ES-VAE’s z_5 focuses on the elbow. Overall, ES-VAE seems to decompose gait variability in a way that separates individual limbs more cleanly.

F Ablation Studies

Effect of different alignments. Table 6 shows the benefit of progressively stronger geometric alignment. On NTU-60, Macro F1 improves steadily from 0.26 without alignment to 0.56 under full alignment, while on the stroke dataset RMSE decreases from 5.75 to 2.82. Notably, translation removal alone is insufficient for stroke severity regression, whereas the major gains appear after removing scale and rotation, with the best performance achieved by the fully aligned Kendall + TSRVF representation.

KL weight β_{kl} . We swept β_{kl} over dataset-specific ranges for both the stroke and NTU-60 datasets (Table 7). In both cases, intermediate KL weights gave the best trade-off between latent regularization and downstream performance: for the stroke dataset, $\beta_{kl} = 2^{-3}$ achieved the best R^2 , while for NTU-60, $\beta_{kl} = 10^{-4}$ gave the highest Macro F1. Larger β values made the latent space more Gaussian but degraded reconstruction and predictive performance, whereas very small β values could lead to weakly regularized or partially collapsed latent dimensions.

Table 6: Alignment ablation with ES-VAE across the NTU activity-recognition dataset and the stroke dataset. Values are point estimates of F1 and RMSE with raised 95% confidence intervals in parentheses.

Alignment stage	NTU-60 Macro F1	Stroke RMSE
No alignment	0.26 ^(0.22–0.31)	5.75 ^(5.00–6.38)
Translation removal (centering)	0.45 ^(0.41–0.49)	6.01 ^(5.37–6.57)
Translation + scale removal (preshape)	0.46 ^(0.42–0.50)	5.72 ^(5.24–6.13)
Translation + scale + rotation removal (Kendall)	0.52 ^(0.47–0.56)	3.13 ^(2.65–3.53)
Full alignment (Kendall + TSRVF)	0.56 ^(0.52–0.60)	2.82 ^(2.29–3.21)

Table 7: Effect of the KL-weight β_{kl} on ES-VAE performance for NTU-60 action recognition and the stroke dataset.

Metric	NTU-60 Macro F1					Stroke R^2				
	10^{-5}	10^{-4}	10^{-3}	10^{-2}	10^{-1}	2^{-5}	2^{-4}	2^{-3}	2^{-2}	2^{-1}
Value	0.544	0.556	0.535	0.466	0.351	0.737	0.737	0.740	0.737	0.727

Tangent-space MSE vs. geodesic reconstruction loss. Replacing the geodesic reconstruction loss with a tangent-space MSE reconstruction loss reduced performance on both datasets, from 0.56 to 0.53 Macro F1 on NTU-60 and from 0.740 to 0.718 in stroke R^2 . This indicates that geodesic reconstruction provides a consistent, though modest, advantage over a Euclidean tangent-space reconstruction objective in the ES-VAE setting.

G Broader Impact

The experiments and modeling of elastic shape latent space in this work offer new ways for skeleton pose trajectory processing and contributes to the advancement of activity recognition and motion assessment of patients and different participants. It may have positive societal impact by improving interpretable analysis of skeleton pose trajectories for rehabilitation, activity recognition, and automated motion assessment. In clinical settings, compact latent representations of gait may help clinicians quantify mobility impairment, monitor rehabilitation progress, and identify motion patterns that are difficult to summarize manually. However, if used without consent, skeleton motion data could reveal sensitive health or activity information about a person. Therefore, this type of model should be used carefully, with privacy protection, clinical oversight, and validation on diverse groups of participants.